Characterization of the structural response of a lithiated SiO_2 / Si interface
A reactive molecular dynamics study

Verners, O.; Simone, A.

DOI
10.1016/j.mechmat.2019.04.001

Publication date
2019

Document Version
Final published version

Published in
Mechanics of Materials

Mechanics of Materials 136 (2019) 103030

Contents lists available at ScienceDirect

Mechanics of Materials

journal homepage: www.elsevier.com/locate/mechmat

Characterization of the structural response of a lithiated SiO_2 / Si interface: A reactive molecular dynamics study

O. Verners[*,a], A. Simone[a,b]

[a] Faculty of Civil Engineering and Geosciences, Delft University of Technology, Delft, the Netherlands
[b] Department of Industrial Engineering, University of Padova, Padua, Italy

ARTICLE INFO

Keywords:
Composite cathode
Structural battery
Silicon
Silicon oxide
Molecular dynamics

ABSTRACT

We report the results of a computational study regarding the mechanical properties of a lithiated Si/SiO_2 interface using reactive molecular dynamics. The study is motivated by an intended application of SiO_2-coated Si nanotubes as fibers in structural batteries with a fiber-reinforced composite architecture while serving as anodes. According to the results, main failure properties due to partly irreversible bond breakage during mechanical deformation are identified, indicating agreement with bond energy/bond order based estimates. Microscopic failure properties are also identified and interpreted in view of the observed processes of bonding degradation. In particular, the effect of Li distribution on the shear deformation response is evaluated as significant.

1. Introduction

Structural power composites are considered as a possible solution for the integration of structural and power storage components in portable electronic devices and vehicles (Asp et al., 2015; Sairajan et al., 2016). To this end, the solid polymer electrolyte-coated fiber architecture (Leijonmarck et al., 2013), applicable to three-dimensional fiber-in-a-matrix microbatteries (Dunn et al., 2008), has been explored as an alternative to conventional, laminate based layouts (Wong et al., 2007; Gasco and Feraboli, 2014; Asp and Greenhalgh, 2014; Asp et al., 2015). Considering that a detailed knowledge of the structural failure properties of battery component materials and their interfaces is critical for a successful design and implementation of both types of architectures, this paper reports the findings of a reactive molecular dynamics (MD) study on the dependence of failure properties that are pertinent to SiO_2-coated Si-nanotube anodes, which will be referred to as "double-walled Si-nanotube anodes" in this paper, on Li concentration at the active material-coating interface during structural loading. The chosen approach of MD modeling, beside providing micromechanical insights, is intended as a reference study for computational mechanics modeling of lithiated SiO_2/Si interfaces at larger scales. In particular, it may replace phenomenological or empirical constitutive relations for the description of mechanical properties at the interface.

Wu et al. (2012) have experimentally investigated anode structures, consisting of a silicon nanotube as the active material, encapsulated in an ion-permeable silicon oxide shell. According to the study, the outer surface of the silicon nanotube is constrained to the oxide shell which effectively prevents an outward expansion of the nanotube. The deformation of the silicon due to lithiation is accommodated by its inward expansion in a region that is not exposed to the electrolyte. This geometrical configuration therefore results in a stable solid-electrolyte interphase. We point out that the confinement effect results from a mismatch between lithiation-induced volume change and the stiffness differences of Li_XSi and Li_YSiO_2.[1] Due to it, the Li_XSi volume change is accommodated primarily by an expansion in the inward radial direction of the nanotube. Nonetheless, no detachment between Si and SiO_2 due to lithiation is reported. The coated nanotube architecture by Wu et al. (2012) has been generalized to two- and three-dimensional periodic structures in this study in the schematic setup shown in Fig. 1. The inward expansion approach has also been followed by Fu et al. (2014) and Xu et al. (2014), who have studied the lithiation-induced expansion of Si nanoparticles dispersed in a porous-carbon nanofiber matrix, where the encapsulation of Si in the C chambers is reported to provide space for lithiation.

The focus of the study is on Li concentration effects on interface debonding due to shear deformation failure of the anode (in the simulations we make reference to the interface region in Fig. 1b). The results also allow a qualitative assessment of the differences between

* Corresponding author.
E-mail addresses: o.verners@tudelft.nl (O. Verners), angelo.simone@unipd.it, a.simone@tudelft.nl (A. Simone).

[1] In the remainder of the manuscript, unless noted otherwise, X designates the stoichiometric fraction of Li in Li_XSi, and Y represents the stoichiometric fraction of Li in Li_YSiO_2, which, according to the analysis of a computational study of lithiated glassy silica (Ostadhossein et al., 2016) employing the same force field, corresponds to a mixture of Li_2Si and $LiSi_2O_5$ phases.

https://doi.org/10.1016/j.mechmat.2019.04.001
Received 19 January 2019; Received in revised form 16 March 2019; Accepted 3 April 2019
Available online 17 April 2019

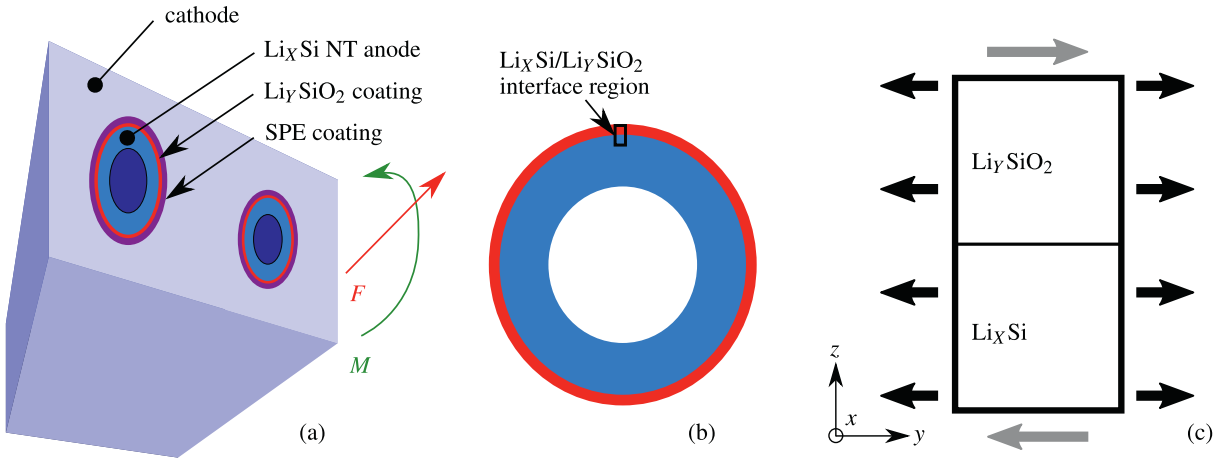

Fig. 1. Anode structure: (a) fiber-matrix architecture and typical mechanical loading (F is the tensile force, M is the bending moment); (b) position of the studied generalized interface region within a nanotube; and (c) deformation modes that represent the main deformation components in bending and stretching of a fiber in the composite (gray arrows designate shear, black arrows designate tension; $X, Y \in [0, 5]$, where X is the stoichiometric fraction of Li in lithiated Si and Y is the stoichiometric fraction of Li in lithiated SiO_2).

electrochemical and mechanical failure properties of the anodes. Furthermore, a quantitative estimation of mechanical failure properties in terms of Li concentration is provided. To this end, the presence of nanoscale size effects—absent or less pronounced under bulk conditions—is shown to be decisive for failure resistance properties at the interface.

The results of this study enable an evaluation of the requirements for compatibility of electrochemical and structural performance of the anode components for applications in structural power composites. The motivation for the evaluation is based on the assumption that different mechanisms account for structural failure related to mechanical loading and battery cycling. According to previous computational studies, another assumption is that Li-caused oxide softening contributes to reduced stiffness (Ostadhossein et al., 2016; Kim et al., 2016), increased ductility (Ostadhossein et al., 2016) and enhanced failure resistance if a gradient in Li-concentration is formed at the interface (Kim et al., 2016). Moreover, it is expected that deviations from a linear rule of mixtures (Sections 3.2 and 3.3) should occur due to the observed nonlinearities in the open circuit voltage (OCV) response of lithiated Si. In this regard, Popov et al. (2011) have found that the nonlinearity of the open circuit voltage response stems from phase transformations, including crystalline-to-amorphous and amorphous-to-crystalline phase transformations, at different Li loading levels (details about phase transformation phenomena in this study are further discussed in Section 2.1).

2. Method

2.1. Material structures and phases

To account for confined boundary conditions due to the assumed tube architecture proposed by Wu et al. (2012), amorphous, lithiated SiO_2/Si structures were generated as described in Section 2.3. Here we refer to the study by Ostadhossein et al. (2015) who used reactive molecular dynamics to investigate the effects of reaction and diffusion-induced stress on the interfacial dynamics and mechanical degradation of crystalline Si nanowire (c-SiNW) anodes under chemo-mechanical lithiation. According to the study, lithiation induces compressive stress at the amorphous-crystalline interface film, causing retardation or even the stagnation of the reaction front. Consequently, due to only amorphous material phases being considered in this study, a locally uniform distribution of Li in Li_XSi can be assumed. At variance, Popov et al. (2011) have computationally established that, with an increase in the lithium concentration, intermediate amorphous Li_XSi phases, up to the crystalline $Li_{15}Si_4$ phase, form in crystalline silicon. We note that no formation of crystalline phases of Li_XSi was observed in our results, which is attributed to the relatively small timescale and room temperature conditions of the simulations. We assume that the formation of crystalline Li_XSi phases at the interface could imply a stress reduction due to a corresponding reduction in material volume.

Further, we refer to the DFT analyses by Rahaman et al. (2016) who have investigated the role of oxygen in silicon suboxide properties. Their results indicate that oxygen atoms interact strongly with the inserted Li atoms, resulting in disintegration of the host matrix. Moreover, a higher concentration of oxygen atoms in the mixture is reported to reduce its relative expansion upon lithiation and increase the lithium storage capacity. The relatively high initial open circuit voltages are assumed to be linked to the formation of stable complexes, such as Li_2O and silicate oxidation products, which may result into reversible capacity loss. Consequently, partly irreversible Li_XSiO_2 phases, corresponding to a saturated lithiation state of SiO_2, were assumed in this study.

To estimate the effect of Li-ion concentration on the shear failure at the interface (Fig. 2), pre-lithiated Li_XSi/Li_5SiO_2 ($X \in [0, 5]$) films were used as interface-forming components. Additionally, Si/SiO_2, $Si/Li_{2.5}SiO_2$, $Li_{2.5}Si/Li_{2.5}SiO_2$, and Li_5Si/Li_5SiO_2 films were produced for estimating the effect of Li-ion concentration on elastic properties under in-plane tension at the interface (the concentrations correspond to the

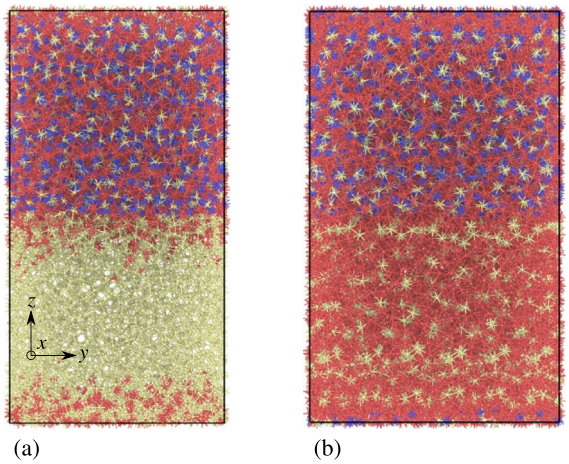

Fig. 2. Sample structures: equilibrium configurations with initial stoichiometries of (a) Si/Li_5SiO_2 and (b) Li_5Si/Li_5SiO_2 structures (Li ●, O ●, Si ●).

state before pre-equilibration). The number of atoms in a system ranged between ≈ 11000 for Li-free structures and ≈ 17000 for fully lithiated structures. We emphasize that, due to the absence of pre-defined structural defects, *e.g.*, cracks or internal voids, the considered structures represent a theoretical upper limit of structural integrity and, consequently, the observed failure properties can be attributed to the maximum strength of the interfaces. The propagation of failure zone after initiation of defects is considered compatible with failure mechanisms that would occur in structures with pre-defined defects.

2.2. Nanoscale boundary conditions

Due to the size of the double-walled Si nanotubes (tube diameter ≈ 400 nm before cycling and thicknesses of about 10 nm and 20 nm for the SiO_2 and Si shells (Wu et al., 2012), respectively), we assume that a size one order of magnitude smaller (< 10 nm) is sufficient for deploying boundary conditions of periodic two-dimensional, chemically bonded films. The assumption is subject to the conditions that cylindrical symmetry can be approximated by translational symmetry due to the small thickness-to-diameter ratio of the tube (≈ 0.075 (Wu et al., 2012)), and outer and inner surface effects are not significant due to the thickness of the nanotube walls. The employed simplification of the structure was motivated both by focus on the localized properties at the Li_X/Li_YiSiO_2 interface and the computational limitation due to prohibitively large size of the nanotube cross-sections. Furthermore, for full-scale SiNT simulations, multiscale continuum methods could be considered (this is discussed in Section 1).

To determine a minimum size for the periodic slab components, initial cubic dimensions of ≈ 15/30/45 Å, obtained by expansion of periodic unit cells of lithiated materials, were used. The criterion for determining the minimum slab thickness was the convergence of the mean of the atomic potential energy in the center of the slab towards the respective bulk value (Section 3.1). For estimates of the respective bulk properties of Li_YSiO_2 ($Y \in [0, 5]$), ≈ 45 × 45 × 45 $Å^3$ periodic cells were used. The film thicknesses after equilibration were 32 ± 13 Å for Li_XSi and 49 ± 9 Å for Li_YSiO_2 in structures for the shear deformation analysis, and 36 ± 3 Å for Li_XSi and 45 ± 5 Å for Li_YSiO_2 in structures for the tensile deformation analysis. The significant dispersion of cell dimensions in shear deformation structures and shrinkage of Li_XSi are considered as a result of structural relaxation and Li diffusion, initiated at the interface (Section 3). In contrast, relatively constant dimensions were obtained for the bulk Li_YSiO_2 cells (43 ± 2 × 46 ± 3 × 46 ± 4 $Å^3$) that were used for the tensile simulations. For structural application purposes, two deformation modes were selected as the main deformation components related to the bending and stretching of fibers (Figs. 1a–c): shear (parallel to the interface plane) and tension (parallel to the fiber axis). Tensile boundary conditions were also imposed on unit cells of lithiated Si for evaluation of the effect of uniaxial strain on the open circuit voltage response. The minimum value of the imposed final strain was determined as the strain that corresponds to material separation in tension and steady state stress in shear. The considered deformation modes may also account for failure of laminar batteries under pinch-torsion conditions, studied both computationally and experimentally at full scale (Vijayaraghavan et al., 2018).

2.3. Simulation settings

Reactive molecular dynamics simulations were performed using the bond length/bond order based MD potential ReaxFF (details of the potential model can be found in van Duin et al. (2001, 2013)) in LAMMPS (Plimpton, 1995) with the USER-REAXC module implementation (full details regarding the implementation can be found in Aktulga et al. (2012)) and a parameter set for Si/O/Li, available as a part of the supplemental information of Ostadhossein et al. (2016). Ostadhossein et al. (2016) and Fan et al. (2013) include validation calculations for equations of state of different Li_YSiO_Z and Li_XSi species, respectively. The latter properties are crucial for reproducing elastic mechanical properties. Additional validation calculations of Li_XSi and SiO_2 Young's moduli have also been performed. The mean (≈ 62 GPa) of complementary two estimates by linear interpolation of the Young's modulus of amorphous Li_4SiO_4 at 91% of its theoretical mass density (2.28 g/cm^3 (Karditsas and Baptiste, 1995)) – 74 GPa (Chu et al., 1988) and 51 GPa (Karditsas and Baptiste, 1995) – indicates sufficient agreement with the value 60.77 GPa according to test simulations at the same density (2.07 g/cm^3 (Kim et al., 2016)). Generally, for both materials an underestimation with respect to the reference data is observed. Considering another study which employs the same Li/Si/O interaction parameters (Fan et al., 2013) and reports quantitative agreement with experimental observations regarding mechanical failure properties of pristine and lithiated Si nanowires at upper limit (attributed to the high strain rates of MD simulations), no complementary DFT validation was necessary.

For the generation of lithiated structures, amorphous Si and SiO_2 unit cells were produced by annealing of 2 × 2 × 2 crystalline Si (diamond cubic) and crystalline SiO_2 (α-quartz) unit cells for 4 (3) cycles at a heating (cooling) rate of 22 (18) K/ps between 300 K and 2500 (2100) K. We note that the obtained melting temperatures of Si (≈ 1100–1400 K, Supporting Information, Fig. S1a) and SiO_2 (≈ 800–1000 K, Supporting Information, Fig. S1b) are notably lower than the reference values (1687 K (RSC, 2018) and 1883-2009 K (PubChem, 2018), respectively). The differences were not considered to be of direct relevance for the present study, since material properties at room temperature were being investigated.

Consequently, cell sizes of 14 ± 1, 8.3 ± 0.4, and 23 ± 13 $Å^3$ for Li_XSi and 13 ± 2, 8.4 ± 0.4, and 12 ± 1 $Å^3$ for Li_YSiO_2 were obtained. The grand canonical Monte Carlo (GCMC) (Frenkel and Smit, 1996) ensemble, in an implementation by Senftle et al. (2014), was employed for the simulations of bulk lithiation. For the MD-equilibration during and after the GCMC simulations, the constant pressure and volume ensemble (NPT) was imposed at 300 K and 1 atm. To obtain dispersion in mass density of sample structures, NPT pre-equilibration simulations were performed at 300, 600, 900, and 1100 K, 1 atm. For increased dispersion in bond order (BO) analysis and cross-thickness property distributions, additional structures were obtained by pre-equilibration at 1300, 1500, 1700, 1900, and 2100 K, 1 atm. The pre-equilibration was performed for 12 ps (2100 K) or 30 ps (other temperatures). The effects of pre-equilibration temperature were assessed by comparing the stiffnesses of the respective structures (Supporting Information, Figs. S2a1,b1). According to the latter, no dependence in form of monotonic reduction on temperature up to ≈ 1000 K was observed, except for specific concentrations of Li in Li_YSiO_2 (Si/$Li_{2.5}SiO_2$ and $Li_{2.5}Si$/$Li_{2.5}SiO_2$). Since all the structures were identified as amorphous, the latter dependence was attributed to interfacial thermodynamics due to the relatively pronounced dependence of mass density and, partly, equilibration-induced changes of Li concentration in Li_YSiO_2 layer on pre-equilibration temperatures above ≈ 500 K (Supporting Information, Figs. S2a2,a3,b2,b3).

Prior to high-temperature pre-equilibration, NPT equilibration at room temperature (300 K/1 atm) was performed for 70–400 ps, depending on the case, for Li_YSiO_2 bulk cells and for 0–250 ps (0 implies that high-temperature equilibration was applied immediately after 0 K energy minimization) for the Li_XSi/Li_YSiO_2 structures. After high-temperature pre-equilibration, 30 ps of room temperature NPT equilibration (300 K/1 atm) were applied. To accelerate Li diffusion across the interface, the 300 K and NPT equilibrated structures were pre-equilibrated at 900 K by imposing the constant volume and temperature (NVT) ensemble conditions. Here we point out that the sampling approach is subject to the assumption that any sample correlation due to identical unit cells, employed for creating the initial structures for pre-equilibration, can be neglected due to the structural dispersion that was generated during pre-equilibration at different temperatures. The

approach also accounts for the inhomogeneities that would occur in larger samples of the materials.

A default cutoff of 5 Å (LAM, 2017) (significantly larger than the considered bond lengths (Ostadhossein et al., 2016)) was used for bonded interactions, and a cutoff of 10 Å was used for the hydrogen bonding interactions (slightly larger than the default value of 7.5 Å (LAM, 2017)). The latter settings were used as conservative estimates for precluding computational artifacts in bonded and long-range interactions, respectively. A Verlet integration timestep of 0.25 fs was used for all simulations except annealing and 2100 K pre-equilibration simulations for which a timestep of 0.1 fs was used. The Nose-Hoover barostat was used for all NPT simulations with a damping constant of 250 fs. The Nose-Hoover thermostat was used for all NVT and NPT simulations with a damping constant of 25 fs, except the annealing simulations for which the Langevin thermostat was used, also with a damping constant of 25 fs.

The tensile deformation was imposed by incrementally scaling the simulation box along the strain direction (Fig. 1c). We point out that, although for the latter deformation mode fully periodic simulation cells were employed, the convergence towards bulk energy in the middle of each film (Section 2.2) was considered sufficient for interpreting the results as representative of the response of the materials at the interface. The deformation was imposed in two directions, parallel to the interface of each sample structure (*xz* and *yz* for shear; *x* and *y* for tension) and thereby eight deformation samples were obtained for each Li concentration level. During tensile loading simulations, lateral dimensions were maintained at 1 atm pressure (NPT ensemble)—the tensile mode represents generalized plane strain conditions. The relaxation of the pressure in lateral directions during tensile simulations was attributed to the finite size of the SiNT architecture. We point out that, due to the employed boundary conditions, the tensile simulations do not allow to obtain the effective stiffness of the SiO_2 layer of nanotubes. For an estimation of the latter, full thickness of the layer and a micromechanical procedure according to, *e.g.*, Vodenitcharova and Zhang (2003), Wang and Zhang (2008), and Vijayaraghavan and Zhang (2018) should be considered.

The shear deformation was imposed by displacing fixed, 5 Å thick outer sublayers of the Li_XSi and Li_YSiO_2 films with respect to each other (Fig. 1c). Due to the effect of nonperiodic boundary conditions in the direction normal to the interface (*z*-direction), the vicinity of fixed-atom films is considered as an approximation of transition to bulk-like properties of the material. Therefore, the estimate of the respective normal stress during shear simulations was not considered for analysis. Likewise, the simulation box shape and volume (NVT ensemble) were preserved. Thereby, the shear mode approximates simple shear and plane strain conditions. Consequently, the Poisson effect was expected to reduce the fracture toughness of structures in shear simulations.

During the simulations of shear and tensile deformation, engineering strain rates of 50 ns^{-1} were imposed. Strain rate effects, discussed in Section 3.1, were estimated by comparing the ultimate stress during dynamic loading against values for NPT equilibrated structures, with deformed dimension fixed at strains of interest and 1 atm equilibration applied in the lateral directions. Identical settings were used for an assessment of the effect of uniaxial strain on the open circuit voltage response of bulk cells of lithiated Si.

2.4. Analysis methods

To analyze the dependence of localized properties on the distance from the interface plane, 20 sampling bins were defined in the direction of the film thickness coordinate (*z*). For an assessment of Li concentration effect on Li_XSi and Li_YSiO_2 bond structures, averaged bond order statistics were used. In particular, the application of a bond order cutoff value of 0.3 effectively limits the estimates to the first coordination shell of each type of pairs of atoms. The bond orders were estimated at each considered Li concentration with the aim of identifying interactions that would account for the microscopically observed behavior of strain-hardening or strain-softening stress response and fracture (Sections 3.2 and 3.3). Specifically, the dependence on Li concentration was considered for the initial state bond orders (total values ΣBO) and their relative change (ΔΣBO) at ultimate strain with respect to initial (tension) and ultimate (shear) stress states—the choice of a reference state for the shear deformation was based on the consideration of a dispersion in stress data that was comparatively large prior to reaching the ultimate stress. Oxide-component bonds in film structures were distinguished by considering atoms that have at least a single O-neighbor (bond order based). A 5 Å transition layer between Li_XSi and Li_YSiO_2 was excluded for film based mass density and stoichiometry calculations.

The zone of main plastic shear deformation was defined as the material film where localization of irreversible shear deformation occurs, with a transition delineated by discretized sublayers (discretization step ≈ 4 Å) in which the spatial derivative of the deformation velocity exceeds a threshold value $(\partial v_y/\partial z)/(\partial v_y/\partial z)_{\max} = 0.2$ (this value was chosen by taking into account the assumed dispersion in data), approaching from the side where no plastic deformation is present.

The open circuit voltage was estimated as

$$V(X) = -\frac{\partial E_f}{\partial X}, \tag{1}$$

where E_f is formation energy and X is the concentration of Li (X in Li_XSi or Li_XSiO_2). The free energy of formation estimate was based on potential energy only, which, consequently, corresponds to ~ 0 K conditions of the materials.

3. Results and discussion

3.1. Equilibration, strain, strain rate, and sample size effects

The film size-effects were estimated by comparing the potential energy distribution for three film sizes at limit concentrations of Li (Section 2.1). According to the energy distributions (Supporting Information, Figs. S3a,b), no significant change was observed for Si. At variance, a slightly lower energy at the interface for the *lithiated* SiO_2 film is attributed to a possible minor densification effect (Fig. 7b). Likewise, for $Li_{5.7}SiO_2$, a small increase in energy at the interface is attributed to a localized reduction of mass density (Fig. 3b). Finally, a larger energy dispersion for $Li_{2.8}Si$ and $Li_{5.7}SiO_2$ films is attributed to phase segregation effects due to lithiation (Ostadhossein et al., 2016; Guo et al., 2008; Yan et al., 2013; Huang and Zhu, 2011). For both limit concentrations, convergence towards the respective bulk values for the largest, ≈ 45 Å thick structures was observed. Consequently, films with an initial thickness of ≈ 45 Å were considered suitable for approximating a transition to bulk-like conditions in the middle of each material film.

For structures with identical initial concentrations of Li in the SiO_2 film (Li_5SiO_2), used in shear deformation simulations, Li diffusion at $X < 2$ from the Li_YSiO_2 film towards the Si film is observed due to a reduction with respect to the initial concentration of Li (Fig. 4a). In contrast, at $X > 2$ Li saturation in the Li_YSiO_2 film is established. In the Li_XSi film, a lower-than-initial concentration of Li was obtained for all structures. Consequently, it is concluded that the interface film accounts for the depletion of Li atoms in the Li_XSi film. Similar trends are observed for the structures that were used in simulations of tensile deformation at $Y \geq 2.5$ (Fig. 4b).

No significant effect of uniaxial deformation on the open circuit voltage of Li_XSi was found (Fig. 5a), the average volume change being $\approx 260\%$ at Li_4Si with respect to diamond cubic Si. The observation is linked to the identical relative volume change for all strain levels (Fig. 5b). For comparison we note that in the present simulations the relative volume change of Li_YSiO_2 due to lithiation is $\approx 90\%$ at Li_5SiO_2 with respect to *α*-quartz. The open circuit voltage result is considered

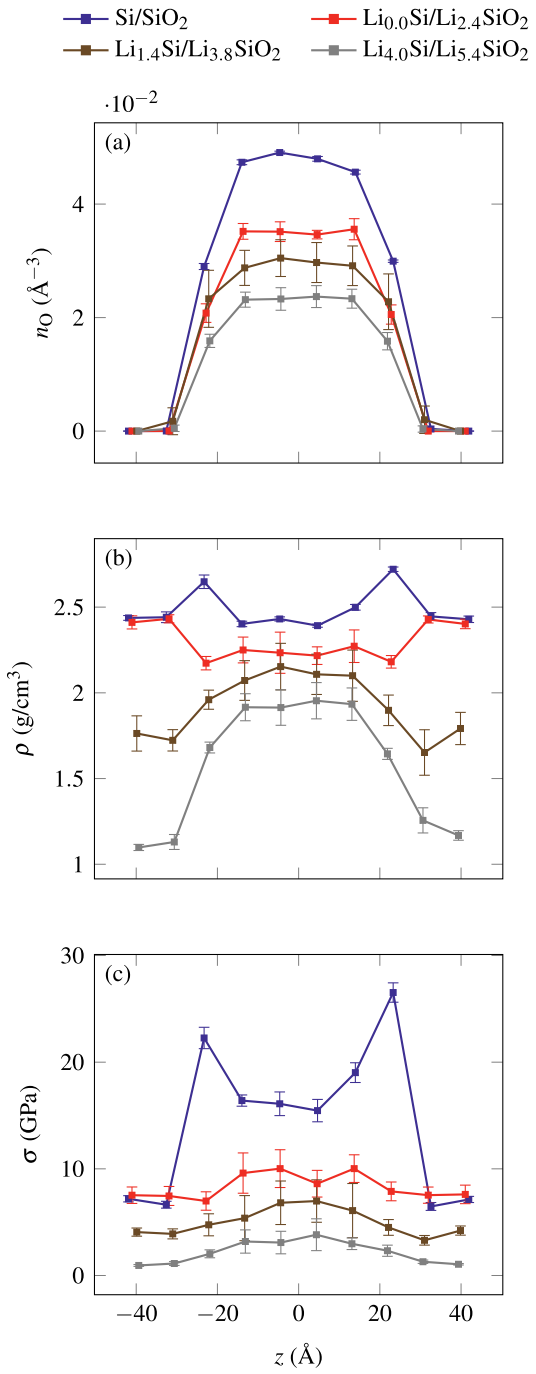

Fig. 3. Film structure and tensile stress distribution: distribution of (a) O number density, (b) mass density, and (c) tensile stress across Li_XSi/Li_YSiO_2 structures in the direction of film thickness coordinate z ($z = 0$ corresponds to the center plane of the SiO_2 film).

relevant for justifying the employed approach of constructing the simulation cells from material films of given Li concentrations (Section 2.1), in addition to the effect of small thickness-to-diameter ratio (Section 2.2). We add that the conclusion is consistent with the observed Li distribution in fully lithiated state of SiO_2-coated Si nanowires under diffusive lithiation conditions according to a previous reactive molecular dynamics study (Figs. 5a1,b1 of Kim et al., 2016), which does not indicate significant differences in Li concentration with respect to non-stressed condition of the respective materials. Further, we note the occurrence of opposite lateral, in-plane stresses in Li_XSi and Li_YSi O_2 films during tension (Supporting Information, Fig. S4). The latter effect is interpreted as a result of mismatch of Poisson's ratios of the materials and, consequently, is regarded as a potential cause of initiation of interfacial cracks.

We add that, according to a comparison of the open circuit voltage against Li concentration (Figs. 5a and Supporting Information, S5), Li_XSi and Li_XSiO_Y phase transformations are assumed to follow previously observed reaction paths (Ostadhossein et al., 2016). We note that a slight, force field related overestimation of Li concentration in lithiated SiO_2, according to current (Supporting Information, Fig. S5) and reference (Ostadhossein et al., 2016) results, is assumed to be present in agreement with experimentally observed reaction sequences (Yan et al., 2013) suggesting a maximum ratio of SiO_2:Li atoms of $\approx 1:4$.

For the tensile loading, an approximately constant stress reduction of ≈ 0.5 due to relaxation is established (Supporting Information, Figs. S6b1, b2). In contrast, for the shear loading, the ratio of dynamic against quasi-static characteristic values of shear stresses (Supporting Information, Figs. S6a1, a2) indicates a monotonic reduction. The difference in relaxation behavior is attributed to the relative changes in principal bond types of pristine materials (62% reduction for Si-Si bonds in Li_XSi, 6% increase for Si-O bonds in Li_YSiO_2), which suggests that the extent of changes in material structure, discussed in Sections 3.2 and 3.3, accounts for the change in strain rate effect. The extent of structural change is found to be consistent with the differences in lithiation-induced density change of Li_XSi (50% reduction, Fig. 6c) and Li_YSiO_2 (21% reduction, Fig. 7b) films.

3.2. Shear deformation analysis

Ideal plastic behavior is observed in the shear stress response after a short range of strain-softening at the lowest Li concentration (Supporting Information, Fig. S7). At higher Li concentrations, significantly less softening occurs, disappearing completely at the maximum Li concentration. Instead, we observe a behavior reminiscent of ideal elasto-plasticity. The reduction, which coincides with an increased strain range that corresponds to the strain-softening, is attributed to a decreasing stiffness with respect to pristine Si (Fig. 6a). We point out that no formation of cracks or voids was observed in the shear deformation simulations. We add that the data in Fig. S7 also serve as the source of stress and strain related results in Fig. 6, similarly to the results in Figs. S8a-c and 7a,b, respectively.

3.2.1. Failure localization

According to the shifts of the plastic deformation zone, characterized by the approximate peak positions of the profiles of shear strain rate, from ≈ -2 Å at $X = 0$ to ≈ 4 Å at $X = 2.0$ (rightmost peak) and to ≈ -15 Å at $X = 4.1$ (leftmost peak), a localized deformation at the interface is observed at $X < 2.5$ (Fig. 8a, where 2.5 is taken as the mean of 2.0 and 2.9). The localization and the initial expansion of the plastic deformation zone are attributed to Li migration towards the Li_YSiO_2 film due to equilibration (Fig. 4a), which decreases the stiffness of Li_XSi at the interface (Fig. 6a). In contrast, a more pronounced plastic deformation zone expansion and relocation towards the Li_XSi film at $X > 2.5$ (Fig. 8b) are interpreted as a result of changing stiffness ratio of the respective materials (Supporting Information, Figures S8a,b) and Li saturation in the Li_YSiO_2 film (Fig. 4b). The latter is, consequently, assumed to contribute to a more homogeneous Li distribution across the Li_XSi film. We note that the discontinuity in plastic deformation zone thickness at $X \approx 2.5$ is regarded as a result of a change in the localization mechanism.

Because of the reduction of yield slip (Fig. 6d), it is concluded that the localized failure strain in the plastic deformation zone decreases during lithiation. Here we add that non-monotonicity of yield slip response is attributed to the uncertainty level in data (discussed in Section 3.2.2). Further, we point out that for the Li-free structure, a distinct plastic deformation zone width could not be established due to

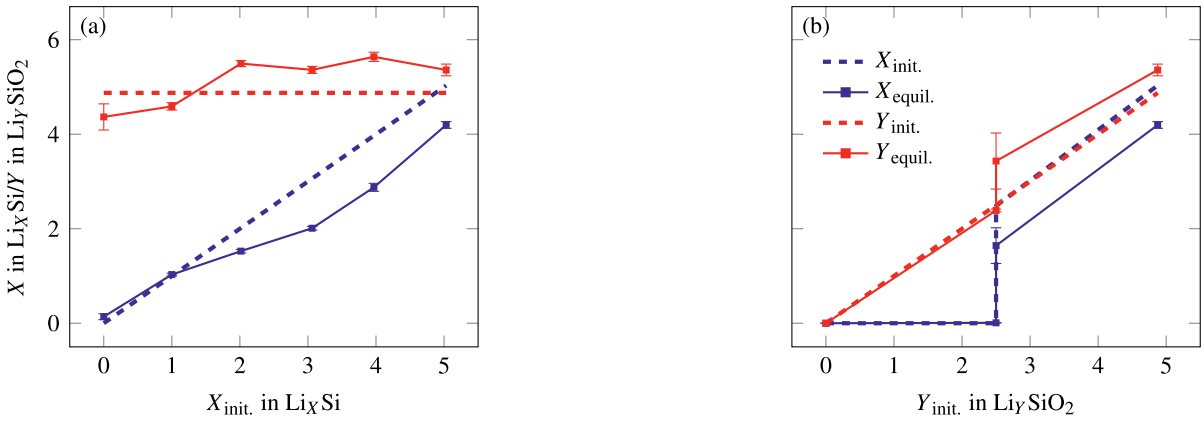

Fig. 4. NPT-equilibrium stoichiometries of films of lithiated Si/SiO_2 structures against initial stoichiometries. The initial stoichiometries correspond to structures obtained during GCMC simulations. The NPT-equilibrated structures were employed in simulations of (a) shear and (b) tensile deformation.

the shear strain being distributed uniformly across the whole thickness of the Si film ($tk_f > 30$ Å). Likewise, at maximum concentration of Li ($Li_{4.1}Si$), a size effect is anticipated due to the width of the plastic deformation zone approaching the thickness of $Li_{4.1}Si$ film. In contrast, the response of the low-concentration structure of $Li_{0.1}S/Li_{4.2}SiO_2$ indicates highly localized plasticity. Consequently, a small further increase in the plastic deformation zone width is predicted also for lithiated Si interface regions due to the likely increase in the homogeneity of Li distribution after larger timescale equilibration and the observed size effect.

3.2.2. Stiffness and strength

A further insight into the structural behavior is gained by considering the relation between atomistic and microscopic properties. First, a qualitatively similar monotonic reduction due to lithiation is observed for mass density, stiffness, strength, and the initial sum of Si-Si bond orders in the Li_XSi film (Figs. 6a–c, Supporting Information, S9a,b). Furthermore, a reduction in slope for all quantities at $X \approx 1.5$ coincides with a change in the response of the open circuit voltage against Li concentration in Li_XSi $U(X)$ (Fig. 5a), which has been identified as a transition state between interstitial and structural/volume change facilitated mechanisms of lithiation according to an atomistic simulation study (Huang and Zhu, 2011). Due to the large dispersion in yield slip values, as compared to the respective characteristic stress values, a quantitative effect of Li concentration on yield slip could not be estimated. The dispersion is considered as a result of the highly nonlinear stress response (Sections 3.2 and 3.3) that renders linearity based definitions of the yield strain (Dowling, 2007), from which the slip values are derived, more sample-dependent. Consequently, the result should be viewed as qualitative.

In contrast to an approximately constant growth rate of stoichiometry-normalized initial bond orders (Supporting Information, Fig. S9b), a saturation in volume-normalized initial bond orders of Li-Li and Li-Si is observed at $X \approx 2$ (Supporting Information, Fig. S9a). The change is attributed to the above mentioned activation of volume-change facilitated mechanism of lithiation. According to the largest reductions in relative bond orders (Supporting Information, Figs. S10a,b), the main mechanism of inelastic deformation is linked to Li-Li bond breakage within the plastic deformation zone. A second mechanism, effective at lower Li concentrations ($X < 2$), is attributed to the weakening of Li-Si bonds in the Li_XSi film, which are expected to be significantly stronger than the Li-Li bonds (149 kJ/mol and 105 kJ/mol (Luo, 2007), respectively). Likewise, the insignificant change in Si-Si bond energy in the Li_XSi film is interpreted as a result of comparatively large (310 kJ/mol (Luo, 2007)) bond energy. Furthermore, a small increase in Li-$Si_{a\text{-}Si}$ bond orders (Supporting Information, Fig. S10a) and Li-Li_{SiO_2} bond orders (Supporting Information, Fig. S10b) at $X > 2$ is regarded as a strengthening process, related to plasticity-induced relaxation of bonds and an expansion of the plastic deformation zone towards the Li_XSi film (Fig. 8a). Last, we point out that the large dispersion in relative bond orders is seen as an outcome of relatively small change (compared to tensile response according to Fig. S14).

3.3. Tensile deformation analysis

3.3.1. Stiffness and strength

Qualitatively similar monotonic reduction of mass density, stiffness, and O-Si bond orders due to lithiation of the Li_YSiO_2 film is observed up to the saturation limit at $Y = 5$ (Figs. 7a,b, Supporting Information,

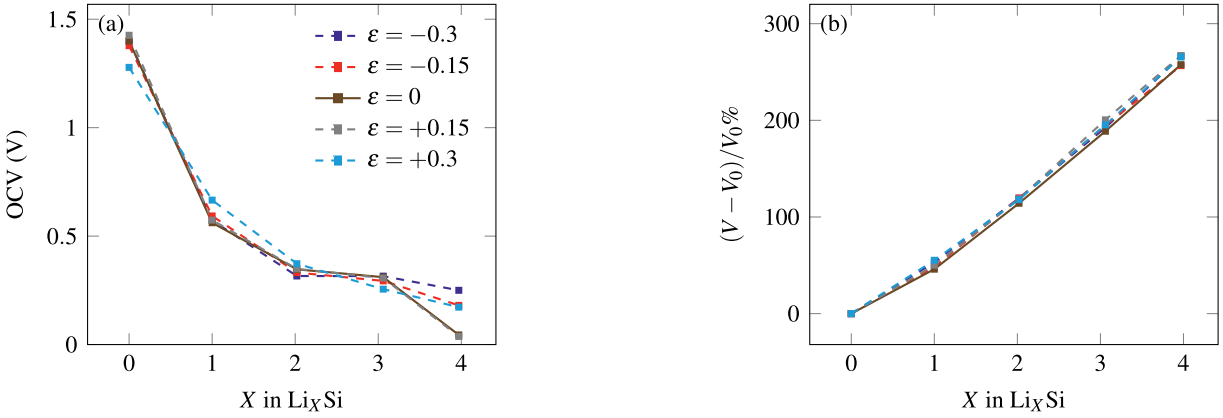

Fig. 5. Uniaxial strain effects: comparison of (a) the open circuit voltage (with respect to Li/Li^+) and (b) mass density of Li_XSi at different uniaxial strain (ε) levels.

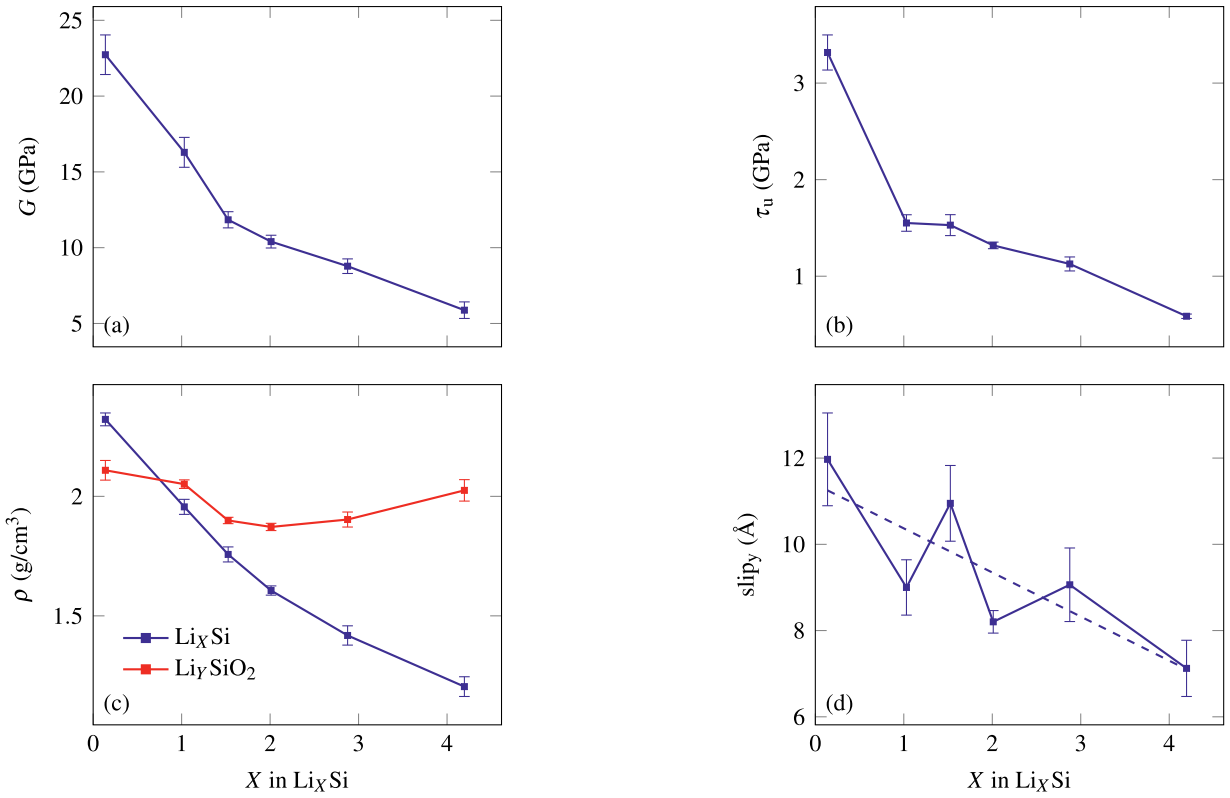

Fig. 6. Shear response characteristics: dependence of (a) mean shear stiffness, (b) mean shear strength, (c) Li_XSi and Li_YSiO_2 film mass densities, and (d) yield slip on Li concentration in Li_XSi/Li_YSiO_2 structures.

Figs. S13a,b). Here we point out that, generally, O-Si bonds contribute significantly to the material's strength due to relatively high bond energies compared to O-Li and Li-Li (799.6 kJ/mol, 340.5 kJ/mol, and 105 kJ/mol (Luo, 2007), respectively). Furthermore, a comparison of film stress responses (Supporting Information, Figs. S8a,b) indicates significant differences in stiffness between the Li_XSi and Li_YSiO_2 films at all Li concentrations. The differences are slightly increased by significantly lower reduction in density of the Li_YSiO_2 films compared to the Li_XSi films due to lithiation (Fig. 7b). The latter difference is attributed to the comparatively high stability of Li silicate compounds (discussion of the results reported by Rahaman et al., 2016 in Section 2.1). Consequently, the fracture of Li_YSiO_2 film is considered as the principal mechanism of axial tensile failure at interface. The fracture is facilitated by void formation, which coincides with local distortion of the material (Supporting Information, Figs. S11 and S12). We note that for thin (< 5 Å) SiO_2 coatings of Si nanowires, the fracture is observed to be predominantly normal to the direction of maximum principal strain (Kim et al., 2016), which suggests that dissipation of most of the deformation energy in form of microscopically brittle fracture may be expected.

At this point we refer to the computational study by Kim and Qi (2014) on the open circuit voltage, elastic properties, and Li-ion diffusion characteristics in polycrystalline SiO_2 and Al_2O_3, and their lithiated compounds. According to the study, lithiation slightly stiffens SiO_2. The opposite—softening—effect of Li on SiO_2 has been established for amorphous material phases (Kim et al., 2016; Ostadhossein et al., 2016) and is confirmed by this study.

The change in material structure is characterized by a monotonic increase in stoichiometry-normalized initial bond orders of Li-Li and Li-O up to $Y \approx 5$ (Supporting Information, Fig. S13b). The change in slope of BO(X) is attributed to a Li saturation effect (Supporting Information, Fig. 4b). Further, the bond based failure of Li_YSiO_2 film is attributed

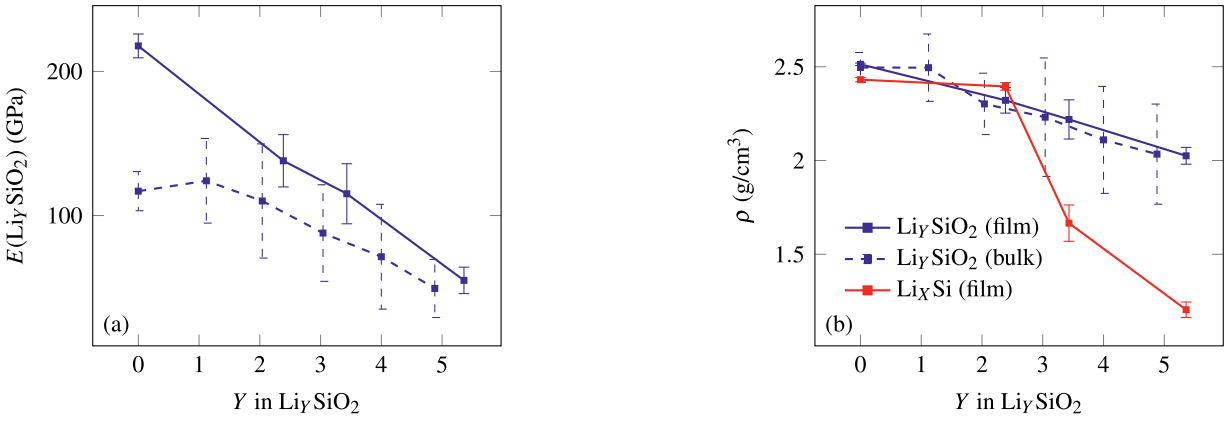

Fig. 7. Tensile response characteristics: dependence of (a) stiffness and (b) mass density of the Li_YSiO_2 film on Li concentration.

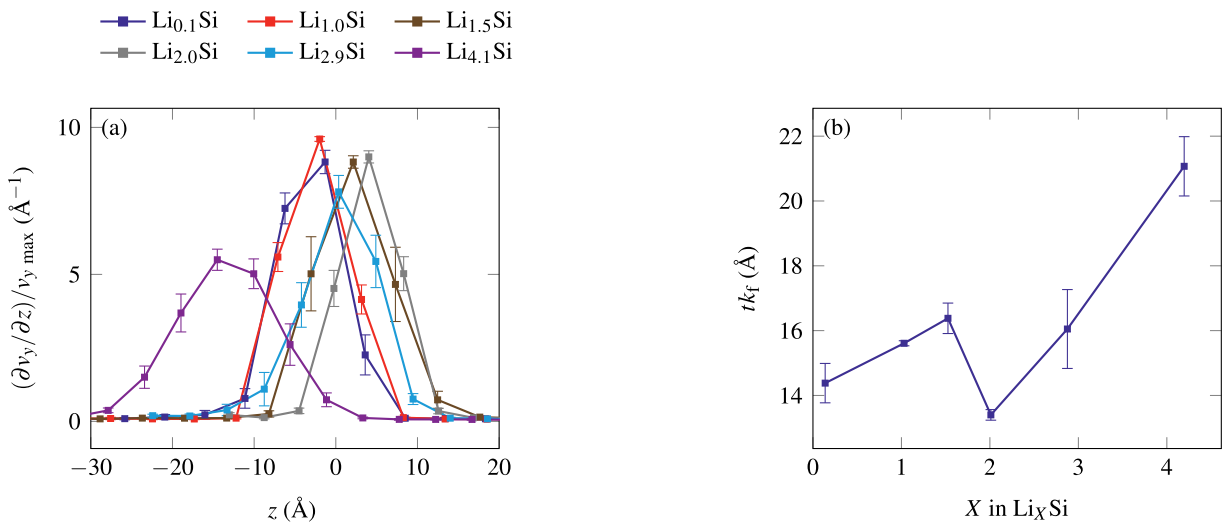

Fig. 8. Inelastic shear strain distribution: dependence of (a) distribution of shear strain rate across Li_XSi/Li_YSiO_2 interfaces ($z < 0$ corresponds to Li_XSi; $z > 0$ corresponds to Li_YSiO_2) and (b) estimate of thickness of plastic shear deformation zone at Li_XSi/Li_YSiO_2 interfaces on Li concentration.

primarily to the degradation of Li-Li and O-Si bonds (Supporting Information, Fig. S14). Moreover, the significant difference in stiffness of bulk and interface Li_YSiO_2 at low Li concentrations (Fig. 7a) is attributed to the pronounced $\sigma(\varepsilon)$ nonlinearity of the interface structures as compared to the bulk material (Supporting Information, Fig. S8c). In particular, it is considered as a result of nonuniform stress and mass density distribution at the interface (Supporting Information, Figs. 3b,c), which indicates a significant reduction of both quantities towards the center of the film. Consequently, it is concluded that the $\approx$ 20 Å thick transition layer between the two materials accounts primarily for the overall difference of tensile response of bulk and interface Li_YSiO_2 phases. Considering that the maximum stress localization coincides with a drop in O atom concentration (Supporting Information, Fig. 3a), the observation is considered to be also affected by the difference in stiffness of bulk Si and SiO_2, the average stiffness of α-quartz (95.4 GPa (Pabst and Gregorova, 2013)) being significantly lower than that of diamond cubic Si (130–188 GPa (Hopcroft et al., 2010)).

A distinct change in slope of Li_XSi film density against Y at $Y \approx 2.5$ (Fig. 7b) is found to coincide with a change in X against Y (Fig. 4b). Similar changes are observed in stiffness properties at the same Li concentration (Figs. 7a). Consequently, considering that the particular Li concentration coincides with a change in the open circuit voltage response of bulk Li_YSiO_2 (Supporting Information, Fig. S5), the change is attributed to a known multistep reaction pattern (Yan et al., 2013; Ostadhossein et al., 2016). In particular, a transition between Li_4SiO_4/Si and Li_4/Si formation is anticipated according to a reactive molecular dynamics study (Ostadhossein et al., 2016).

4. Summary and conclusions

A negligible effect of uniaxial deformation on the open circuit voltage of bulk Si is observed at all lithiation levels. Thereby, an insignificant effect of mechanical loading on the open circuit voltage can be predicted for double-walled Si nanotube based anodes, employed as fibers in structural power composites.

It is confirmed that Li reduces stiffness and strength of both component materials at the interface, similarly to the respective bulk materials. Furthermore, the observed plastic shear localization indicates an increased delamination possibility for $X < 2.5$ in Li_XSi. In contrast, a reduction of shear strain gradient occurs for $X > 2.5$ in Li_XSi due to an expansion of plastic shear zone.

The results highlight failure properties that are dependent on Li concentration and may initiate structural failure of the interface within double-walled Si nanotube anodes—delamination in shear/bending—earlier than in Li-free structures. Moreover, the observed improvements of interfacial failure resistance due to lithiation (expanded plastic deformation zone in shear) suggest that high concentration of Li reduces the interfacial fracture probability compared to low concentration.

To improve the delamination resistance of these interfaces in view of the obtained results, possible alternatives could be a higher mass density and, consequently, stiffness of the transition layer. The requirement could be fulfilled, *e.g.*, by forming a suboxide transition layer, which would correspond to a gradual variation of material properties across the interface (as in functionally graded materials).

Since, according to our results, a number of nanoscale effects are confirmed to contribute to a structural failure at the interface, we consider the knowledge of the respective bulk and free surface properties of component materials as insufficient for reliable predictions of interfacial failure behavior under conditions of perfect initial bonding. Consequently, the approach of this contribution can be considered appropriate for obtaining realistic upper limit interface properties.

Acknowledgments

The research leading to these results has received funding from the European Research Council under the European Union's Seventh Framework Programme (FP7/2007-2013) / ERC Grant agreement no. 617972.

Supplementary material

Supplementary material associated with this article can be found, in the online version, at doi:10.1016/j.mechmat.2019.04.001.

References

Aktulga, H.M., Fogarty, J.C., Pandit, S.A., Grama, A.Y., 2012. Parallel reactive molecular dynamics: numerical methods and algorithmic techniques. Parallel Comput. 38 (4–5), 245–259.
Asp, L.E., Greenhalgh, E.S., 2014. Structural power composites. Compos. Sci. Technol. 101, 41–61.
Asp, L.E., Leijonmarck, S., Carlson, T., Lindbergh, G., 2015. Realisation of structural battery composite materials. Proceedings of the 20th International Conference on Composite Materials (ICCM20). Copenhagen, Denmark.
Chu, C.Y., Poeppel, R.B., Singh, J.P., Goretta, K.C., 1988. Mechanical properties of solid breeder materials. Technical Report DOE/ER–0313/4. Oak Ridge National Lab.
Dowling, N.E., 2007. Mechanical Behavior of Materials, 3rd edition. Pearson.
van Duin, A.C.T., Dasgupta, S., Lorant, F., Goddard III, W.A., 2001. Reaxff: a reactive force field for hydrocarbons. J. Phys. Chem. A 105 (41), 9396–9409.
van Duin, A.C.T., Zou, C., Joshi, K., Bryantsev, V., Goddard, W.A., 2013. A reaxff reactive

force-field for proton transfer reactions in bulk water and its applications to heterogeneous catalysis. Comput. Catal. RSC Catalysis Ser. 14, 223–243.
Dunn, B., Long, J.W., Rolison, D.R., 2008. Rethinking multifunction in three dimensions for miniaturizing electrical energy storage. Electrochem. Soc. Interface 17 (3), 49–53.
Fan, F., Huang, S., Yang, H., Raju, M., Datta, D., Shenoy, V.B., van Duin, A.C.T., Zhang, S., Zhu, T., 2013. Mechanical properties of amorphous LixSi alloys: areactive force field study. Modell. Simul. Mater. Sci. Eng. 21 (7), 074002.
Frenkel, D., Smit, B., 1996. Understanding Molecular Simulation: From Algorithms to Applications, 1st edition,. Academic Press.
Fu, K., Lu, Y., Dirican, M., Chen, C., Yanilmaz, M., Shi, Q., Bradford, P.D., Zhang, X., 2014. Chamber-confined silicon-carbon nanofiber composites for prolonged cycling life of li-ion batteries. Nanoscale 6, 7489–7495.
Gasco, F., Feraboli, P., 2014. Manufacturability of composite laminates with integrated thin film li-ion batteries. J. Compos. Mater. 48 (8), 899–910.
Guo, B., Shu, J., Wang, Z., Yang, H., Shi, L., Liu, Y., Chen, L., 2008. Electrochemical reduction of nano-siO2 in hard carbon as anode material for lithium ion batteries. Electrochem. Commun. 10 (12), 1876–1878.
Hopcroft, M.A., Nix, W.D., Kenny, T.W., 2010. What is the young's modulus of silicon? J. Microelectromech. Syst. 19 (2), 229–238.
Huang, S., Zhu, T., 2011. Atomistic mechanisms of lithium insertion in amorphous silicon. J. Power Sources 196 (7), 3664–3668.
Karditsas, P.J., Baptiste, M.J., 1995. Thermal and structural properties of fusion related materials. Technical Report UKAEA-FUS–294. UKAEA Government Division.
Kim, S.-Y., Ostadhossein, A., van Duin, A.C.T., Xiao, X., Gao, H., Qi, Y., 2016. Self-generated concentration and modulus gradient coating design to protect Si nano-wire electrodes during lithiation. Phys. Chem. Chem. Phys. 18, 3706–3715.
Kim, S.-Y., Qi, Y., 2014. Property evolution of Al_2O_3 coated and uncoated Si electrodes: a first principles investigation. J. Electrochem. Soc. 161 (11), F3137–F3143.
LAMMPS documentation, 2017. http://lammps.sandia.gov/doc/Manual.html. Accessed 2017-04-26.
Leijonmarck, S., Carlson, T., Lindbergh, G., Asp, L.E., Maples, H., Bismarck, A., 2013. Solid polymer electrolyte-coated carbon fibres for structural and novel micro batteries. Compos. Sci. Technol. 89, 149–157.
Luo, Y.-R., 2007. Comprehensive Handbook of Chemical Bond Energies, 1st edition. CRC Press.
Ostadhossein, A., Cubuk, E.D., Tritsaris, G.A., Kaxiras, E., Zhang, S., van Duin, A.C.T., 2015. Stress effects on the initial lithiation of crystalline silicon nanowires: reactive molecular dynamics simulations using ReaxFF. Phys. Chem. Chem. Phys. 17, 3832–3840.
Ostadhossein, A., Kim, S.-Y., Cubuk, E.D., Qi, Y., van Duin, A.C.T., 2016. Atomic insight into the lithium storage and diffusion mechanism of SiO_2/Al_2O_3 electrodes of lithium ion batteries: ReaxFF reactive force field modeling. J. Phys. Chem. A 120 (13), 2114–2127.
Pabst, W., Gregorova, E., 2013. Elastic properties of silica polymorphs – a review. Ceramics-Silikaty 57 (3), 167–184.
Plimpton, S., 1995. Fast parallel algorithms for short-range molecular dynamics. J. Comput. Phys. 117 (1), 1–19.
Popov, Z.I., Fedorov, A.S., Kuzubov, A.A., Kozhevnikova, T.A., 2011. A theoretical study of lithium absorption in amorphous and crystalline silicon. J. Struct. Chem. 52 (5), 861–869.
Pubchem, 2018. https://pubchem.ncbi.nlm.nih.gov. Accessed 2018-08-25.
Rahaman, O., Mortazavi, B., Rabczuk, T., 2016. A first-principles study on the effect of oxygen content on the structural and electronic properties of silicon suboxide as anode material for lithium ion batteries. J. Power Sources 307, 657–664.
Periodic Table, 2018. http://www.rsc.org/Periodic-table/. Accessed 2018-08-25.
Sairajan, K.K., Aglietti, G.S., Mani, K.M., 2016. A review of multifunctional structure technology for aerospace applications. Acta Astronaut. 120, 30–42.
Senftle, T.P., van Duin, A.C.T., Janik, M.J., 2014. Determining in situ phases of a nanoparticle catalyst via grand canonical Monte Carlo simulations with the ReaxFF potential. Catal. Commun. 52, 72–77.
Vijayaraghavan, V., Garg, A., Gao, L., 2018. Fracture mechanics modelling of lithium-ion batteries under pinch torsion test. Measurement 114, 382–389.
Vijayaraghavan, V., Zhang, L.C., 2018. Effective mechanical properties and thickness determination of boron nitride nanosheets using molecular dynamics simulation. Nanomaterials 8 (7), 546.
Vodenitcharova, T., Zhang, L.C., 2003. Effective wall thickness of a single-walled carbon nanotube. Phys. Rev. B 68, 165401.
Wang, C.Y., Zhang, L.C., 2008. A critical assessment of the elastic properties and effective wall thickness of single-walled carbon nanotubes. Nanotechnology 19 (7), 075705.
Wong, E.L., Baechle, D.M., Xu, K., Carter, R.H., Snyder, J.F., Wetzel, E.D., 2007. Design and processing of structural composite batteries. Proceedings of the Society for the Advancement of Material and Process Engineering (SAMPE) – 2007 Symposium and Exhibition. 52. Baltimore, Maryland
Wu, H., Chan, G., Choi, J.W., Yao, Y., McDowell, M.T., Lee, S.W., Jackson, A., Yang, Y., Hu, L., Cui, Y., 2012. Stable cycling of double-walled silicon nanotube battery anodes through solid-electrolyte interphase control. Nat. Nanotechnol. 7 (5), 310–315.
Xu, Z.-L., Zhang, B., Kim, J.-K., 2014. Electrospun carbon nanofiber anodes containing monodispersed Si nanoparticles and graphene oxide with exceptional high rate capacities. Nano Energy 6, 27–35.
Yan, N., Wang, F., Zhong, H., Li, Y., Wang, Y., Hu, L., Chen, Q., 2013. Hollow porous siO2 nanocubes towards high-performance anodes for lithium-ion batteries. Sci. Rep. 3, 1568.